Spectroscopy of Thulium ions in solid-solution sesquioxide laser ceramics: Inhomogeneous spectral line broadening, crystal-field engineering and C_3i sites

Kirill Eremeev, Pavel Loiko, Stanislav Balabanov, Timofey Evstropov, Dmitry Permin, Olga Postnikova, Valentin Petrov, Patrice Camy, Alain Braud

Spectroscopy of Thulium ions in solid-solution sesquioxide laser ceramics: Inhomogeneous spectral line broadening, crystal-field engineering and C_{3i} sites

Kirill Eremeev,[a] Pavel Loiko,[a] Stanislav Balabanov,[b] Timofey Evstropov,[b] Dmitry Permin,[b,c] Olga Postnikova,[b,c] Valentin Petrov,[d] Patrice Camy,[a] Alain Braud,[a,*]

[a]*Centre de Recherche sur les Ions, les Matériaux et la Photonique (CIMAP), UMR 6252 CEA-CNRS-ENSICAEN, Université de Caen, 6 Boulevard du Maréchal Juin, 14050 Caen Cedex 4, France*

[b]*G. G. Devyatykh Institute of Chemistry of High-Purity Substances of RAS, 49 Tropinin St., 603951 Nizhny Novgorod, Russia*

[c]*N. I. Lobachevsky National Research University, 23 Gagarin Ave., 603022 Nizhny Novgorod, Russia*

[d]*Max Born Institute for Nonlinear Optics and Short Pulse Spectroscopy, Max-Born-Str. 2a, 12489 Berlin, Germany*

**Corresponding author, e-mail: alain.braud@ensicaen.fr*

Abstract: We present a detailed spectroscopic study of Tm^{3+} ions in stoichiometric and "mixed" (solid-solution) cubic (C-type, sp. gr. $Ia\bar{3}$) sesquioxides R_2O_3 (R = Y, Lu, Sc or their mixture), with the goal of developing broadband-emitting gain media for ultrafast lasers at ~2 μm. Evidence of a linear variation (increase) of the crystal-field strength when decreasing the ionic radius of the host-forming cation R^{3+} in the isostructrural R_2O_3 series is presented. The crystal-field splitting of Tm^{3+} multiplets is determined for C_2 sites and justified using a barycenter plot, and the first evidence of C_{3i} Tm^{3+} species is presented. A remarkable inhomogeneous spectral broadening for compositionally "mixed" sesquioxides (in particular such with Sc^{3+}) with respect to the parent compounds is revealed at low temperatures. It is proven that binary and ternary "mixed" R_2O_3 compounds form substitutional solid-solutions with a mixing of the host-forming cations at the atomic level. The stimulated-emission and gain cross-sections for the $^3F_4 \rightarrow {}^3H_6$ Tm^{3+} transition are determined. Guidelines for material engineering of Tm^{3+}-doped gain media for mode-locked 2-μm lasers are also provided.

Keywords: Cubic sesquioxides; transparent ceramics; thulium ions; optical spectroscopy; luminescence; crystal field.

1. Introduction

A sesquioxide is any oxide containing three oxygen atoms for every two atoms of another element. Sesquioxides of rare-earth elements with a chemical formula R_2O_3 (R = Sc – Lu) can crystalize in three different crystal structures: trigonal (type A, sp. gr. *P*3*m*1), monoclinic (type B, sp. gr. *C*2/*m*), and body-centered cubic (type C, sp. gr. $Ia\bar{3}$). The cubic phase in particular is of increasing interest for optical applications.

Cubic sesquioxides R_2O_3 with optically passive host-forming cations R = Y, Lu and Sc (called respectively yttria, lutecia and scandia) are attractive host crystals for doping with laser-active rare-earth ions [1]. As host matrices, they offer (i) good thermal properties, i.e., high thermal conductivity (12.8 $Wm^{-1}K^{-1}$ for undoped Lu_2O_3) with a weak dependence on the rare-earth doping level in the case of similar ionic radii, e.g. Yb^{3+} [2], (ii) weak isotropic thermal expansion and positive thermo-optic coefficients [3] leading to positive thermal lensing, (iii) low phonon energies among oxide crystals (e.g., 612 cm^{-1} for Lu_2O_3) [4], (iv) a broad transparency range, and (v) possible high rare-earth doping levels. In addition, the dopant ions in R_2O_3 crystals experience strong crystal-fields leading to large total Stark splitting of their multiplets and, consequently, broadband emission properties. A particular feature of cubic sesquioxides is the sensitivity of their crystal-field strengths to the host-forming cations leading to a significant variation of the spectroscopic properties in the R = Y → Lu → Sc series [5]. The low phonon energy of R_2O_3 crystals determines weak rates of multiphonon non-radiative relaxation from the excited states of the dopant ions [6].

Cubic R_2O_3 sesquioxides (R = Y, Lu and Sc) adopt the bixbyite structure (bixbyite is the $(Fe,Mn)_2O_3$ mineral), $^{VI}[R_2]^{IV}[O_3]$, where $^{VI}[]$ and $^{IV}[]$ are octahedral and tetrahedral sites, respectively [7]. The corresponding lattice constants are a = 10.596 Å, 10.391 Å and 9.857 Å. This structure is derived from the fluorite lattice by doubling the lattice parameter and leaving 1/4 of the anion sites vacant in an ordered way. A fragment of the crystal structure of yttria [8] is shown Fig. 1(a). The unit-cell contains 32 cation sites of which 24 exhibit the C_2 symmetry (Wyckoff: 24*d*) and the remaining 8 ones – the C_{3i} symmetry (Wyckoff: 8*b*), Fig. 1(b). For both sites, the R^{3+} cations are VI-fold coordinated by oxygens, Fig. 1(c). The bonding is different for the two R^{3+} sites of the C-type structure: the oxygens around R1 form a regular octahedron with 6 equal R−O distances (2.285 Å), while those around R2 form an irregular octahedron with three different R−O distances (2.248, 2.270, 2.335 Å, all the values are specified for Y_2O_3). Each $[R2O_6]$ polyhedron is linked to four $[R1O_6]$ ones via edge-sharing.

For the C_{3i} sites, the electric dipole (ED) transitions are forbidden due to the presence of a center of inversion, and only magnetic dipole (MD) transitions are allowed. Thus, rare-earth ions residing in these sites practically do not contribute to transition intensities. For the C_2 sites, both the ED and MD transitions are allowed.

Thulium ions (Tm^{3+}) possess an electronic configuration of $[Xe]4f^{12}$ with a ground-state $^3H_6$. They are known for a broadband emission in the eye-safe spectral range around 2 μm owing to the $^3F_4 \rightarrow {}^3H_6$ electronic transition. They offer intense and broad absorption at ~0.8 μm (to the $^3H_4$ state), this spectral range being well addressed by commercial high power AlGaAs diode lasers [9,10]. The pump quantum efficiency for Tm^{3+}-doped materials can approach 2 (a “two-for-one” pump process) because of an efficient cross-relaxation (CR)

between adjacent Tm^{3+} ions, $^3H_4 + {}^3H_6 \rightarrow {}^3F_4 + {}^3F_4$ [11]. 2 μm Tm-lasers are of practical importance for LIDAR systems (range finding, atmosphere gas sensing, wind mapping), medical applications, soft material processing and frequency down-conversion into mid-infrared.

Cubic R_2O_3 sesquioxides are extremely suitable for Tm^{3+} doping [4]. They feature large Stark splitting of the Tm^{3+} ground-state ($^3H_6$) leading to a very broad emission extending well beyond 2 μm [12] thus avoiding the water vapor structured absorption present in the atmospheric air which is essential for generation of femtosecond pulses from mode-locked oscillators [13,14], long upper laser level ($^3F_4$) lifetimes leading to a low-threshold laser behavior [15] and efficient CR [16]. Efficient and power-scalable $Tm:R_2O_3$ lasers have been reported [4,17].

Auzel *et al.* proposed a scalar crystal field strength parameter N_v to compare different materials in terms of the Stark splitting (ΔE) of $4f^n$ multiplets of rare-earth ions $^{2S+1}L_J$, as $\Delta E(^{2S+1}L_J) \sim N_v$ [18]. Thus, by plotting the total Stark splitting of one manifold of a particular rare-earth ion vs. that of another manifold of the same ion, one can compare the crystal-field strength for different crystalline materials. Such an analysis is performed in Fig. 2 for the case of Tm^{3+} ions, by plotting ΔE of the first excited-state ($^3F_4$) vs. that of the ground-state ($^3H_6$). One can see that for oxide matrices, the crystal-field strengths and the corresponding Stark splittings are in general higher. Among the oxide hosts, the cubic R_2O_3 crystals feature one of the largest crystal-field strengths and, more remarkably, a pronounced sensitivity to the nature of the host-forming cation R^{3+} (the total Stark splitting gradually increases in the R = Y → Lu → Sc series). Thus, they are indeed among the best candidates for achieving broadband emission using the $^3F_4 \rightarrow {}^3H_6$ transition by engineering of their composition.

Cubic sesquioxides can form substitutional solid solutions in the $Y_2O_3 – Lu_2O_3 – Sc_2O_3$ ternary system, i.e., $(Y_{1-x-y}Lu_xSc_y)_2O_3$ for the whole range of $0 \leq x, y \leq 1$ [19]. Such compositionally "mixed" materials feature an inhomogeneous broadening of absorption and emission bands of the dopant ions [20,21] as their second coordination spheres are composed of R^{3+} cations with different sizes. Due to the particularly strong sensitivity of the crystal-field strength for the dopant rare-earth ions in sesquioxides to the host-forming R^{3+} cations, the effect of "mixing" is expected to be strong for these materials. The spectral broadening can lead to smooth, broad and nearly structureless gain spectra supporting the generation of ultrashort pulses. Thus, such "mixed" sesquioxides are of primary importance for the development of mode-locked lasers [14,22] and amplification of their output.

Transparent polycrystalline ceramics are optical materials composed of μm-sized randomly oriented closely packed single-crystalline grains featuring weak light scattering. Usually, cubic materials are used for the transparent ceramic technology. Thus, cubic sesquioxides appear very suitable for fabricating laser ceramics [23]. The advantages of sesquioxide laser ceramics with respect to the corresponding single-crystals are: (i) lower synthesis temperatures (<1800 °C), (ii) easier rare-earth doping (better control of the actual ion density, higher available doping levels and more uniform ion distribution), (iii) the possibility to fabricate "mixed" compositions $(R_1,R_2)_2O_3$ with well controlled R_1/R_2 ratios and (iv) size scalability. The thermal and spectroscopic properties of sesquioxide ceramics greatly resemble

those of single-crystals. Note that the growth of single-crystals with some of the solid-solution compositions has also been reported [24,25].

Recently, Tm^{3+}-doped "mixed" sesquioxide ceramics such as $(Lu,Sc)_2O_3$ and $(Y,Lu)_2O_3$ enabled generation of ultrashort (sub-100 fs) pulses at wavelengths slightly above 2 μm [14,22]. Further development of mode-locked Tm-sesquioxide ceramic lasers requires a deep understanding of the relationship between the host composition, the crystal-field strengths and the resulting inhomogeneous spectral broadening for Tm^{3+} ions in sesquioxide ceramics within the Y_2O_3 – Lu_2O_3 – Sc_2O_3 system. The existing spectroscopic studies focus on a few particular compositions without giving a general picture on this topic.

In the present work, we aim to establish the relations between the host composition and the spectroscopic properties of Tm^{3+} ions in cubic sesquioxide solid-solutions within the Y_2O_3 – Lu_2O_3 – Sc_2O_3 system.

2. Synthesis of ceramics

A series of sesquioxide ceramics, including stoichiometric Y_2O_3, Lu_2O_3, Sc_2O_3, and binary/ternary solid-solutions with equal molar ratio of the metals, $(Lu,Y)_2O_3$, $(Lu,Sc)_2O_3$, and $(Y,Lu,Sc)_2O_3$, doped with 3.0 at.% Tm^{3+}, were fabricated. The initial nanopowders were prepared by the glycine-nitrate method. First, commercial powders of Tm_2O_3 (purity: 4N), Y_2O_3, (5N), Lu_2O_3 (4N), Sc_2O_3 (4N) from Polirite, Russia were dissolved in nitric acid (6N, Khimreaktiv, Russia), the corresponding nitrates were mixed, and glycine (3N, Khimreaktiv, Russia) was added in a 1:1 mole ratio. After drying the solution, the precursor was placed in a furnace heated up to 500 °C. The combustion reaction resulted in the formation of nanodispersed powders of $Tm:R_2O_3$. The powders were calcined at 900°C for 5 h in air and compacted in a steel mold with a diameter of 13 mm at a pressure of 250 MPa. The green bodies were sintered at 1780 °C for 3 h in an oil vacuum lower than 1×10^{-2} Pa. The furnace was equipped with a tungsten rod as a heating element and graphite thermal insulation. The samples were then annealed in air at 1000 °C for 10 h to restore the oxygen stoichiometry. The obtained transparent ceramics had a slight coloration due to the Tm^{3+} doping.

All the ceramics were of single-phase nature (C-type, sp. gr. $Ia\bar{3}$) as confirmed by X-ray powder diffraction (XRD). The bixbyite-type structure of sesquioxides is well documented [26]. In Fig. 3(a), a close look at the most intense diffraction peak related to the (222) Bragg reflection is shown. For the parent compounds, the position of the most intense diffraction peak related to the (222) Bragg reflection, see Fig. 3(a), progressively shifts to higher diffraction angles 2θ in the R = Y → Lu → Sc series. For the "mixed" compounds, this diffraction peak takes an intermediate position between those for the corresponding parents. This behavior is due to a nearly linear relation between the average ionic radius of the host-forming cation R^{3+} (for VI-fold oxygen coordination) [27] and the lattice constant *a*, expressed by the Vegard's law [28], see Fig. 3(b).

The Tm^{3+} ion density N_{Tm} was 8.06, 8.55 and 9.92 [10^{20} at/cm^3] for the parent compounds (Y_2O_3, Lu_2O_3 and Sc_2O_3, respectively) and 8.37, 8.92 and 8.67 [10^{20} at/cm^3] for the "mixed" ones ($(Y,Lu)_2O_3$, $(Lu,Sc)_2O_3$ and $(Y,Lu,Sc)_2O_3$, respectively).

3. Results and discussion

3.1. Raman spectra

Raman spectroscopy is a sensitive tool for studying material structures and their possible alteration. The vibronic properties of parent R_2O_3 sesquioxides (R = Y, Sc, Nd – Lu) are well known [4]. In the present work, Raman spectroscopy was employed to confirm the formation of substitutional solid-solutions for "mixed" sesquioxide ceramics. The Raman spectra of parent Tm:R_2O_3 ceramics (for R = Y, Lu and Sc) are shown in Fig. 4(a). They agree with the spectra reported previously by Abrashev *et al.* for powders of undoped Y_2O_3, Lu_2O_3 and Sc_2O_3 [4]. For cubic (C-type) sesquioxides with a body-centered structure, the factor group analysis predicts the following set of irreducible representations for the optical and acoustical modes at the center of the Brillouin zone Γ ($\boldsymbol{k} = 0$): $\Gamma_{op} = 4A_g + 4E_g + 14F_g + 5A_{2u} + 5E_u + 16F_u$ and $\Gamma_{ac} = F_u$, of which 22 *gerade* modes (A_g, E_g and F_g) are Raman-active, 16 modes (F_u) are IR-active and the rest are silent [29,30]. The measured spectra are characteristic for cubic sesquioxides. The most intense Raman peak is assigned to $A_g + F_g$ vibrations. In the R = Y → Lu → Sc series, its position shifts to higher energies (377.8 → 391.4 → 416.8 cm^{-1}) and its width broadens (full width at half maximum, FWHM: 6.2 → 7.3 → 8.4 cm^{-1}). A similar tendency is observed for all the assigned Raman peaks, in particular, for the maximum phonon energy ($F_g + A_g$ vibrations, 593 → 612 → 667 cm^{-1}).

Figure 4(b) shows a close look at the dominant Raman peak for all six studied compounds. For the "mixed" ceramics, it takes an intermediate position between those for the parent ones and notably broadens. The latter effect is more pronounced for Sc^{3+}-containing ceramics due to the smaller ionic radius of Sc^{3+} (0.745 Å) as compared to those of Y^{3+} (0.90 Å) and Lu^{3+} (0.861 Å, all values correspond to a VI-fold coordination by oxygen). For example, for Tm:$(Y,Lu)_2O_3$ and Tm:$(Lu,Sc)_2O_3$, the dominant Raman peak is found at 385.4 and 405.1 cm^{-1} and its FWHM is as broad as large as 12.8 and 31.2 cm^{-1}, respectively. This confirms the formation of a substitutional solid-solution.

The dependence of the dominant Raman peak energy with the average ionic radius of the host-forming cation R^{3+} in Tm:R_2O_3 is shown in Fig. 4(c). The experimental points are well fitted with a linear law.

The comparison of the Raman spectra of Tm^{3+}-doped yttria and scandia single-crystals and polycrystalline ceramics is shown in Fig. 4(d). For yttria compounds, the spectra are very close, while for the scandia ones, the dominant Raman band in ceramic slightly broadens and experiences a minor shift to lower energies as compared to the corresponding single crystal.

3.2. Absorption spectra

The absorption spectra of Tm^{3+} ions in the parent sesquioxide *crystals* Y_2O_3, Lu_2O_3 and Sc_2O_3 were reported [5]. In the present work, we focus on the spectral line broadening for Tm^{3+} ions in "mixed" sesquioxide ceramics, while the spectra for parent ceramics are mainly provided for comparison.

The absorption cross-sections, σ_{abs}, were calculated as α_{abs}/N_{Tm}, where α_{abs} is the absorption coefficient, i.e., accounting for the total density of the dopant Tm^{3+} ions. Two transitions were considered, $^3H_6 \rightarrow {}^3H_4$ and $^3H_6 \rightarrow {}^3F_4$. The first one is commonly used for

pumping Tm^{3+} ions, as already mentioned, by commercial high-power AlGaAs laser diodes emitting around 0.8 μm. The second one is promising for in-band pumping (directly to the upper laser level), e.g., by Raman-shifted Erbium fiber lasers operating at 1.68 μm.

The σ_{abs} spectra for the parent compounds are shown in Fig. 5(a,c). In the R = Y → Lu → Sc series, the peak absorption cross-sections slightly increase, the absorption bands (as a whole) broaden while the individual peaks related to particular electronic transitions become narrower. For the $^3H_6 \rightarrow {}^3H_4$ transition, the peak σ_{abs} is 0.37×10^{-20} cm^2 at 796.7 nm ($Tm:Y_2O_3$), 0.38×10^{-20} cm^2 at 796.2 nm ($Tm:Lu_2O_3$) and 0.40×10^{-20} cm^2 at 795.8 nm ($Tm:Sc_2O_3$) and the absorption linewidth (FWHM) is 4.2, 3.5 and 3.4 nm, respectively. These data agree well with the previous study for Tm^{3+}-doped Y_2O_3, Lu_2O_3 and Sc_2O_3 single-crystals [5,25].

For "mixed" compounds, cf. Fig. 5(b,d), the absorption spectra become less structured and this effect is stronger for Sc^{3+}-containing ceramics. The spectra of solid-solutions cannot be obtained simply as a linear combination of the spectra of the two corresponding parents (as shown in Fig. 5(b) by a dashed curve for the case of $Lu_2O_3 – Sc_2O_3$). As a result, the peak σ_{abs} values decrease while the corresponding absorption linewidths increase (in part because of the merging of several individual absorption peaks). This behavior is favorable for reducing the sensitivity to the temperature drift of the emission wavelength of AlGaAs diode lasers. For the $^3H_6 \rightarrow {}^3H_4$ transition, the peak σ_{abs} amounts to 0.33×10^{-20} cm^2 at 796.2 nm ($Tm:(Y,Lu)_2O_3$) and 0.29×10^{-20} cm^2 at 792.2 nm ($Tm:(Lu,Sc)_2O_3$) and the absorption linewidth is ~21 nm. It is worth noting that the ternary ceramic $Tm:(Y,Lu,Sc)_2O_3$ does not provide much smoother spectra than the $Tm:(Lu,Sc)_2O_3$ one.

The broadening degree of the absorption spectra correlates adequately with the difference between the ionic radius of Tm^{3+} (0.88 Å) and the mean ionic radius of the host-forming R^{3+} cations (0.881, 0.835 and 0.803 Å for R = (Y,Lu), (Y,Lu,Sc) and (Lu,Sc), respectively).

The results on the peak absorption cross-sections for the $^3H_6 \rightarrow {}^3H_4$ Tm^{3+} transition in all six studied ceramics are summarized in Table 1.

3.3. Emission (spectra and lifetimes)

The stimulated-emission (SE) cross-sections, σ_{SE}, for the $^3F_4 \rightarrow {}^3H_6$ transition of Tm^{3+} ions in the parent sesquioxide *crystals*, Y_2O_3, Lu_2O_3 and Sc_2O_3, were reported [5]. Recently, Kränkel *et al.* [25] and Moncorgé *et al.* [31] overviewed the emission properties of Tm^{3+}-doped binary "mixed" sesquioxides. In the present work, the σ_{SE} spectra for the $Tm:R_2O_3$ ceramics (R = Y, Lu, Sc or their mixture) were calculated using a combination of the reciprocity method (RM) and the Füchtbauer – Ladenburg (F-L) formula.

The Füchtbauer-Ladenburg formula reads [32]:

$$\sigma_{SE}(\lambda) = \frac{\lambda^5}{8\pi \langle n \rangle^2 \tau_{rad} c} \frac{W'(\lambda)}{\int \lambda W'(\lambda) d\lambda}, \quad (1)$$

where, λ is the emission wavelength, $\langle n \rangle$ is the refractive index at the average emission wavelength, τ_{rad} is the radiative lifetime of the emitting level ($^3F_4$ Tm^{3+} state), c is the speed of light, and $W'(\lambda)$ is the luminescence spectral intensity corrected for the spectral response of the detection set-up. In Eq. (1), it is assumed that the luminescence branching ratio is unity which

is true for the $^3F_4 \rightarrow {}^3H_6$ transition. The refractive indices were calculated using dispersion formulas from [33].

The expressions for the reciprocity method read [34]:

$$\sigma_{SE}(\lambda) = \sigma_{abs}(\lambda)\frac{Z_l}{Z_u}\exp\left(-\frac{(hc/\lambda) - E_{ZPL}}{kT}\right), \quad (2a)$$

$$Z_{l(u)} = \sum_k g_k^{l(u)} \exp(-E_k^{l(u)}/kT). \quad (2b)$$

In these equations, h is the Planck constant, k is the Boltzmann constant, T is the temperature (room temperature), E_{ZPL} is the zero-phonon-line (ZPL) energy corresponding to transitions between the lowest Stark sub-levels of the involved multiplets ($^3F_4$ and $^3H_6$ Tm^{3+} manifolds), $Z_{l(u)}$ are the partition functions of the lower (l, $^3H_6$) and upper (u, $^3F_4$) manifolds, $g^{l(u)}_k = 1$ is the degeneracy of Stark sub-levels as expected for monoclinic C_2 sites, and $E^{l(u)}_k$ is the energy of Stark sub-levels measured from the lower-lying sub-level of each multiplet (k is numbering the sub-levels). The data on the crystal-field splitting from Section 3.4 were used.

For each compound, the σ_{SE} spectra were calculated using both methods. The F-L method relying on the measured luminescence spectrum can be inaccurate at shorter wavelengths, in the spectral range with a stronger overlap with the reciprocal absorption band, due to the effect of reabsorption. The calculation via RM fails at longer wavelength due to the exponential term in Eq. 2(a). The radiative lifetime of the $^3F_4$ state was adjusted until a good matching between the spectra calculated by both methods was observed.

The resulting σ_{SE} spectra of Tm^{3+} ions in the parent compounds are shown in Fig. 6(a). In the R = Y → Lu → Sc series, the stimulated-emission cross-section peak increases, and the emission bandwidth increases. The maximum σ_{SE} amounts to 0.92×10^{-20} cm^2 at 1933.5 nm ($Tm:Y_2O_3$), 0.94×10^{-20} cm^2 at 1943.0 nm ($Tm:Lu_2O_3$) and 1.01×10^{-20} cm^2 at 1990.1 nm ($Tm:Sc_2O_3$). The $^3F_4 \rightarrow {}^3H_6$ Tm^{3+} transition represents a quasi-three-level laser scheme with reabsorption. Consequently, the laser emission will occur at wavelengths longer than the ZPL position, i.e., in the long-wave part of the σ_{SE} spectrum, above 2 μm. All three parent sesquioxides present a distinct emission peak in this spectral range. The corresponding SE cross-sections are 0.35×10^{-20} cm^2 at 2051.6 nm ($Tm:Y_2O_3$), 0.32×10^{-20} cm^2 at 2064.4 nm ($Tm:Lu_2O_3$) and 0.39×10^{-20} cm^2 at 2113.7 nm ($Tm:Sc_2O_3$). These results are in line with the previous study for Tm^{3+}-doped Y_2O_3, Lu_2O_3 and Sc_2O_3 single-crystals [5].

For "mixed" sesquioxides, the emission spectra become less structured (the behavior is very similar to that observed for the absorption spectra), see Fig. 6(b). This effect is most pronounced for $Tm:(Lu,Sc)_2O_3$. The SE cross-sections relevant for laser operation are listed in Table 1.

Figure 6(c) shows a close look at the long-wave emission peak (at wavelengths above 2 μm) of Tm^{3+} ions in all six sesquioxide ceramics. This part of the spectrum is particularly attractive for the development of mode-locked lasers delivering femtosecond pulses. This is because multiple narrow absorption lines of water in the atmosphere which appear at shorter wavelengths prevent the generation of such broadband pulses [35]. By selecting the proper host-forming cation R^{3+} (for parent compounds) or their combination (for "mixed" ones), it is possible to tailor both the peak position and the emission bandwidth. For "mixed" compounds,

the peak emission wavelength takes an intermediate position between those for the corresponding parents while the spectral profile of the emission peak broadens. For example, for Tm:$(Lu,Sc)_2O_3$, σ_{SE} is 0.26×10^{-20} cm^2 at 2095.7 nm and the corresponding emission bandwidth (FWHM) is 69.8 nm, compared with 58.1 nm (Tm:Lu_2O_3) and 64.1 nm (Tm:Sc_2O_3).

In this way, Sc^{3+}-containing sesquioxides can provide emission at wavelengths typical for Ho^{3+} ions ($^5I_7 \rightarrow {}^5I_8$ transition) in oxide crystals, thus avoiding the Tm^{3+},Ho^{3+} codoping scheme suffering from strong heat loading [36].

The long-wave emission of Tm^{3+} ions in cubic sesquioxides extending until at least 2.2 μm is most likely due to multiphonon-assisted (vibronic) processes [37,38].

The gain cross-sections, $\sigma_{gain} = \beta\sigma_{SE} - (1-\beta)\sigma_{abs}$, where $\beta = N_2/N_{Tm}$ is the inversion ratio and N_2 the population of the upper laser level ($^3F_4$), were calculated as shown in Fig. 7. For all the sesquioxide ceramics, the gain profiles are broad and naturally extend beyond 2 μm. The position of the long-wave maximum in the gain spectra shifts to longer wavelengths in the R = Y → Lu → Sc series. As expected for the "mixed" ceramics, the spectra become less structured. For small inversion ratios, a local peak above 2 μm dominates in the gain spectra and when increasing β above 0.06–0.08 (depending on the composition), another peak at shorter wavelengths (<2 μm) appears. The long-wave peak above 2 μm is of interest for ultrashort pulse generation. It is due to transitions to the two higher-lying Stark sub-levels of the $^3H_6$ ground-state. As the total Stark splitting and, in particular, the energy position of these two sub-levels is sensitive to the host-forming cation R^{3+} in the sesquioxide host matrix, the maximum in the gain profiles can be precisely controlled by selecting the host composition. The gain bandwidth can be increased for the "mixed" compounds. Figure 8 presents a direct comparison of the gain profiles of Tm^{3+} ions in the R_2O_3 ceramics for the same inversion ratio (β = 0.06) focusing on the spectral range of 2000-2250 nm relevant for the development of femtosecond lasers.

The RT luminescence decay curves from the $^3F_4$ state of Tm^{3+} ions in the Tm^{3+}-doped R_2O_3 ceramics (R = Y, Lu, Sc or their mixture) were measured under resonant excitation, as shown in Fig. 9. The $^3F_4 \rightarrow {}^3H_6$ transition is of purely electric dipole nature and thus only Tm^{3+} ions residing in C_2 sites contribute to the observed emission. The decay curves exhibit a shape characteristic for a decay in the presence of an energy-transfer. These are the phonon-assisted energy-transfer upconversion (ETU) processes from the $^3F_4$ state, namely $^3F_4 + {}^3F_4 \rightarrow {}^3H_6 + {}^3H_4$ (ETU_1) and $^3F_4 + {}^3F_4 \rightarrow {}^3H_6 + {}^3H_5$ (ETU_2) [39].

For low-doped (0.3 at.% Tm^{3+}) parent sesquioxides, the intrinsic luminescence lifetimes $\tau_{lum,0}$ are 3.73 ms (Tm:Lu_2O_3), 3.58 ms (Tm:Y_2O_3) and 3.44 ms (Tm:Sc_2O_3). For ceramics with 3 at.% Tm, the luminescence lifetimes are shortened due to concentration-quenching. With increasing the Sc^{3+} content in the ceramics, τ_{lum} is shortened which is assigned to increased non-radiative path owing to the higher phonon energy of scandia.

Table 2 summarizes the intrinsic luminescence lifetimes ($\tau_{lum,0}$) obtained for ceramic and crystals [5] with a low doping level of ≤ 0.3 at.% Tm, as well as the radiative lifetimes (τ_{rad}) calculated using the Judd-Ofelt theory assuming that only ions residing in C_2 sites (3/4 of ions) contribute to optical absorption [31]. The $^3F_4$ Tm^{3+} manifold for the parent sesquioxides, Y_2O_3, Lu_2O_3 and Sc_2O_3, is considered. The intrinsic lifetimes for ceramics and single-crystals are in

good agreement with each other indicating an almost negligible effect of possible defects and impurity centers in ceramics. They are also in line with the radiative ones evaluated recently by Moncorgé *et al.* [31].

3.4. Low-temperature spectroscopy: parent compounds

Tm^{3+} ions in cubic sesquioxides can reside in two non-equivalent sites with symmetry C_2 (24*d*, 3/4 of cationic positions in the unit-cell) and C_{3i} (8*b*, 1/4 of the cationic positions) [40,41]. Both sites have a VI-fold oxygen coordination. For both sites, each $^{2S+1}L_J$ multiplet with an integer J is split into a total of 2J + 1 Stark sub-levels. The spectroscopic signatures of the C_{3i} sites are expected only for transitions with a MD contribution. We use the phenomenological notations for Tm^{3+} multiplets proposed by Gruber *et al*. [42], namely Z, Y, X and A for the $^3H_6$, $^3F_4$, $^3H_5$ and $^3H_4$ manifolds, respectively. Each Stark sub-level is designated as Z_i, Y_i, X_i and A_i, where i = 1, 2, ... 2J + 1, counting from the lowest sub-level. The assignment of electronic transitions takes into consideration the previous studies [42].

The experimental crystal-field splitting for Tm^{3+} ions in three parent sesquioxides, Y_2O_3, Lu_2O_3 and Sc_2O_3, was reported in PhD theses from University of Hamburg [44,45], however, without providing the low-temperature spectra and their assignment. Moreover, the possible spectroscopic signatures of C3i sites were not analyzed.

First, the low-temperature (LT, 12 K) absorption and emission spectra of Tm^{3+} ions in the three parent sesquioxides (Y_2O_3, Lu_2O_3 and Sc_2O_3) were measured focusing on the four lower-lying multiplets ($^3H_6$, $^3F_4$, $^3H_5$ and $^3H_4$), see Fig. 10.

The LT absorption spectra for the $^3H_6 \rightarrow {}^3F_4$, $^3H_5$ and $^3H_4$ transitions are plotted versus the photon energy ($h\nu_{abs}$, in cm^{-1}). Assuming that only the lowest Stark sub-level of the ground-state is populated, the energies of assigned electronic transitions directly give the Stark sub-level energies. For these multiplets, all the 2J + 1 sub-levels of Tm^{3+} ions in C_2 sites were identified. Then, the LT $^3F_4 \rightarrow {}^3H_6$ emission spectra were measured to determine the splitting of the ground-state and plotted versus E_{ZPL} – photon energy ($Y_1 - h\nu_{lum}$, in cm^{-1}). Again, all 2J + 1 sub-levels of the ground-state of Tm^{3+} ions in C_2 sites were identified.

To reveal the spectroscopic evidence of Tm^{3+} ions in C_{3i} sites, we additionally studied two emissions with a MD contribution, namely $^3H_4 \rightarrow {}^3F_4$ (at ~1.5 μm) and $^3H_4 \rightarrow {}^3H_5$ (at ~2.3 μm). The corresponding LT emission spectra gave access to the Stark splitting of the terminal levels, $^3F_4$ and $^3H_5$, for ions located in both C_2 and C_{3i} sites. The LT emission spectra were plotted versus E_{ZPL} – photon energy ($A_1 - h\nu_{lum}$, in cm^{-1}). Let us first discuss the $^3H_4 \rightarrow {}^3F_4$ emission representing the fingerprints of both the C_2 and C_{3i} sites. By overlapping it with the $^3H_6 \rightarrow {}^3F_4$ transition in absorption (related exclusively to C_2 sites), one can observe narrow extra lines due to the C_{3i} sites. Note that their energy is determined assuming that the lowest Stark sub-level of the $^3H_4$ manifold (A_1) has the same energy for both sites. The full set of 9 sub-levels of the $^3F_4$ state (C_{3i} sites) is determined only for Tm^{3+} ions in Lu_2O_3 and for other compounds, less lines are indentified, namely 8 ($Tm:Y_2O_3$) and 6 ($Tm:Sc_2O_3$).

Now, let us discuss the $^3H_4 \rightarrow {}^3H_5$ emission. It is of both ED and MD nature and thus Tm^{3+} ions located in both the C_2 and C_{3i} sites contribute to it. The transition in absorption giving access to the $^3H_5$ state is also allowed for both sites. By comparing the spectra, one can

identify the extra lines owing to the C_{3i} sites. Moreover, their energy is unambigiously determined from the LT absorption spectrum. A total of 4 extra lines (out of 9 possible Stark sub-levels) are identified in all three compounds. This is the first direct observation of C_{3i} species for Tm^{3+}-doped sesquioxides. Gruber *et al.* calculated the position of Stark sub-levels of the Tm^{3+} ground-state ($^3H_6$) in Y_2O_3 based on the phenomenological crystal-field parameters [41]. However, they cannot be accessed experimentally as the only possible suitable transition, $^3H_4 \rightarrow {}^3H_5$, corresponds to a very weak emission due to the short lifetime of the $^3H_5$ state quenched as a result of the non-radiative relaxation.

Table 2 summarizes the determined energies of Stark sub-levels for Tm^{3+} ions in C_2 sites (full set) and C_{3i} sites (only $^3F_4$ and $^3H_5$ multiplets, partially) for the parent sesquioxides.

We also compared the LT spectra of Tm^{3+} ions in parent single-crystals and ceramics. The the LT $^3H_6 \rightarrow {}^3F_4$ absorption was analyzed for Tm:Y_2O_3 and Tm:Sc_2O_3, similarly to the analysis performed for the Raman spectra. Figure 11 shows a close look at the part of the LT absorption spectrum related to transitions from the $Z_1(^3H_6)$ sub-level to the Y_4 to $Y_9(^3F_4)$ ones. For both compounds, the peak positions are very close (within the measurement error) while the peak width is different. It almost does not change between the Tm:Y_2O_3 single crystal and ceramic while it notably increases between the Tm:Sc_2O_3 ones. We assume that it can be caused by a gradient of the dopant ion concentration in rare-earth-doped Sc_2O_3 by a large difference of the ionic radii of the dopant and host-forming cations [43].

Antic-Fidancev *et al.* proposed the so-called barycenter plot: a plot of the barycenter energy of one $^{2S+1}L_J$ $4f^n$ multiplet of a rare-earth ion vs. that of another multiplet of the same ion, and applied it to the case of several rare-earth ions, namely Nd^{3+} ($4f^2$), Pr^{3+} ($4f^3$), Eu^{3+} ($4f^6$) and Yb^{3+} ($4f^{13}$) ions [46,47]. We applied it here to the case of Tm^{3+} ions. The separation between the $^3H_6$ (ground-state) and $^3F_4$ (first excited-state) manifolds results from the spin–orbit interaction. For Tm^{3+} ions embedded in a crystalline lattice, two different effects can potentially affect this energy separation: (i) the modification of the spin–orbit coupling constant which is weak for 4f transitions of rare-earth ions, and (ii) *J*-mixing (mixing of states with different total angular momentum *J* by the crystal-field) increasing the energy separation between the two manifolds. For Tm^{3+} ions, due to the large energy difference between the $^3H_6$ and $^3F_4$ states (about 5600 cm^{-1}), the *J*-mixing can be neglected. Consequently, we can consider that the energy separation between the Tm^{3+} ground and first excited states is nearly constant for different hosts, and equal to the spin–orbit splitting for the free ion. The barycenter plot can serve as a verification tool for the determined crystal-field splitting. In the present work, we have used this concept to position the determined experimental Stark splittings for Tm^{3+} ions in C_2 sites in R_2O_3 sesquioxides with respect to other materials accommodating Tm^{3+} ions.

3.5. Low-temperature spectroscopy: "mixed" compounds

The LT absorption / emission spectra of Tm^{3+} ions in "mixed" ceramics were studied to reveal the inhomogeneous spectral broadening induced by the compositional disorder. For the sake of brevity, we focus here on one transition relevant for the development of 2 μm lasers, namely the $^3H_6 \leftrightarrow {}^3F_4$ transition, both in absorption and emision, see Fig. 13.

In this section, for describing the spectroscopic properties and, in particular, the crystal-field splitting for "mixed" ceramics, we will use the concept of an activator *quasicenter* first introduced by Kaminski [48] to generalize the optical properties of disordered laser materials. By a quasicenter, we mean an ensemble-averaged structure that generalizes properties of several local activator centers that only slightly differ in structure and have very similar Stark splitting of their energy states. In general, the structure and number of separate activator centers depend on the permissible disorder of a crystalline system and on the concentration of its components, including the activator. For compositionally "mixed" (solid-solution) compounds, a quasicenter can be determined with its crystal-field splitting representing a macroscopic average of multiple local activator centers which differ by the actual composition of the second coordination sphere (which, in turn, depends on the concentration of components constituting the solid-solution). It thus represents an intermediate case between the two parent compounds.

At 12 K, the spectral lines assigned to electronic transitions of Tm^{3+} ions in solid-solution ceramics take an intermediate position between those for the corresponding parents while they significantly broaden. Indeed, for the transition between the Stark components $Z_1 \rightarrow Y_2$ (the $^3H_6 \rightarrow {}^3F_4$ intermanifold transition in absorption), the spectral linewidth (defined as FWHM) at 12 K is just 2.0, 2.1 and 6.4 cm^{-1} for the parent compounds $Tm:R_2O_3$ (for R = Y, Lu, Sc, respectively), while it increases to 20.0 and 62.0 cm^{-1} for the solid-solutions $Tm:(Y,Lu)_2O_3$ and $Tm:(Lu,Sc)_2O_3$, respectively. As a result of such broadening, not all of the possible electronic transitions can be unambigiously assigned.

For the studied solid-solution ceramics, the LT spectroscopy did not reveal any signatures of non-equivalent Tm^{3+} spectroscopic species (e.g., the presence of "twinned" absorption or emission lines which could be associated with Tm^{3+} ions sitting in different local environments preferentially composed of one type of the host-forming cations R^{3+}, or profound dependence of the LT luminescence spectra on the excitation wavelength which was tuned across the entire $^3H_6 \rightarrow {}^3H_4$ absorption band with a laser linewidth of <0.1 nm). This confirms the formation of binary and termary substitutional solid-solutions $(R1,R2)_2O_3$ and $(R1,R2,R3)_2O_3$ with mixing of the host-forming cations R^{3+} at the atomic level. The compositional disorder originated from the second coordination sphere of Tm^{3+} ions formed by different sets of $R1^{3+}$ and $R2^{3+}$ ($R3^{3+}$) cations with different masses and ionic radii. These observations confirm the validity of the quasicenter model described above.

For applications of Tm^{3+}-doped sesquioxides in mode-locked lasers, it is relevant to look at the spectral range of the $^3F_4 \rightarrow {}^3H_6$ emission and, in particular, on its long-wave part extending above 2 μm in sesquioxides. It is determined by the total Stark splitting of the Tm^{3+} ground-state, $\Delta E(^3H_6)$. Figure 14(a) summarizes the experimental crystal-field splitting of the $^3H_6$ Tm^{3+} multiplet in the parent $Tm:R_2O_3$ (R = Y, Lu, Sc) sesquioxide ceramics, as well as tentatively determined Stark sub-level energies for Tm^{3+} ions in the solid-solution compositions. Due to the strong imhomogeneous spectral broadening, even at 12 K, we were unable to determine the full set of Stark sub-level energies for the "mixed" ceramics, so that the number of experimental levels is less than the theoretical one. The energy of each individual sub-level, the barycenter energy of the whole multiplet and its total Stark splitting tend to increase with decreasing the average radius of the host-forming cation R^{3+}, i.e., in the R = Y

→ Lu → Sc series for the parent compounds. As a result, the longest wavelength of the purely electronic $^3F_4 \rightarrow {}^3H_6$ transition experiences a progressive red-shift for smaller R^{3+} cations. It is deduced from the energy of the transition between the Stark sub-levels $Y_1 \rightarrow Z_{13}$ and amounts to 2073 nm ($Tm:Y_2O_3$), 2093 nm ($Tm:Lu_2O_3$) and 2149 nm ($Tm:Sc_2O_3$).

Antic-Fidancev *et al.* reported on a linear variation of the crystal-field strength with the ionic radius of the host-forming cation along the lanthanide series (the crystal-field strength increases for smaller cations) for several isostructural crystal families, including orthovanadates $Pr^{3+}:RVO_4$, sesquioxides $Eu^{3+}:R_2O_3$, garnets $Pr^{3+}:R_3Ga_5O_{12}$ [49,50], and Hölsä *et al.* performed a similar theoretical study for oxychlorides ROCl [51]. In the present work, we extend this concept to both parent and solid-solution sesquioxides doped with Tm^{3+} ions with the goal of more flexible control of their emission properties.

To illustrate the inhomogeneous spectral broadening in solid-solution sesquioxides, the diagram of the crystal-field splitting of the ground-state $^3H_6$ and the first excited-state $^3F_4$ of Tm^{3+} ions accounting both for the Stark sub-level position and the spectral line broadening (FWHM) was constucted, Fig. 15.

In Fig. 16, we compare the longest wavelength of a purely electronic transition $^3F_4 \rightarrow {}^3H_6$ (corresponding to transitions from the lowest Stark sub-level of the $^3F_4$ manifold to the highest sub-level of the $^3H_6$ one) for Tm^{3+} ions in various crystals considered for the development of ultrashort-pulse lasers at ~2 μm [52]. Only a few crystal families exhibit strong enough crystal-fields leading to emission peaks owing to electronic transitions extending above 2 μm (while the long-wave phonon sideband of the $^3F_4 \rightarrow {}^3H_6$ emission band can extend well beyond the range of electronic transitions) thus avoiding the structured water vapor absorption in the atmospheric air, namely garnets, sesquioxides, monotungstates and silicates. Compared to other isostructural series, cubic sesquioxides R_2O_3 show the strongest variation of the emission wavelength with the host-forming cation R^{3+}, and the emission wavelength of Tm^{3+} ions in Sc_2O_3 reaches well beyond 2 μm being exceptionally long among other analyzed compounds.

The analysis performed allowed us to draw several conclusions regarding the material engineering and laser potential of different crystal families for the development of gain media for ~2 μm lasers with broadband emission properties:

(i) For shifting the $^3F_4 \rightarrow {}^3H_6$ Tm^{3+} emission spectra towards longer wavelengths, host matrices with small host-forming cations, leading to stronger crystal-fields, shall be selected. For stronger inhomogeneous spectral broadening in solid-solution compositions, it is necessary to select two parents with rather different sizes of their host-forming cations;

(ii) For achieving emission above 2 μm, the most promising parent compounds are cubic sesquioxides (Y_2O_3-type), cubic ordered ($Y_3Al_5O_{12}$-type) and disordered ($Ca_3Nb_{1.5}Ga_{3.5}O_{12}$-type) garnets, tetragonal disordered melilites ($SrGdGa_3O_7$-type), and monoclinic disordered orthosilicates (Y_2SiO_5-type). Note that the latter two compounds have been barely studied for femtosecond lasers at ~2 μm. The spectral broadening in these systems can be enhanced in "mixed" compositions based on small cations as explained above;

(iii) In the garnet family, it is more promising to study "mixed" compounds of the type $A_3(B1,B2)_5O_{12}$ rather than $(A1,A2)_3B_5O_{12}$ due to the larger variation of the crystal-field strength across the isostructural series in the former case;

(iv) By analogy with the case of Sc^{3+}-containing sesquioxides, we suggest that other Sc^{3+}-containing oxides may be attractive for achieving long-wave emission above 2 μm. For example, the recently identified perovskite-type $GdScO_3$ crystal is expected to be promising for Tm^{3+} doping [53].

4. Conclusions

Cubic rare-earth sesquioxides R_2O_3 (where R stands for the host-forming cation, R = Y, Lu, Sc or their mixture) are very attractive hosts for doping with thulium ions for lasers emitting slightly above 2 μm and, in particular, for generation of ultrashort (few-optical-cycle) pulses in this spectral range. Sesquioxides are available in the form of single-crystals and transparent polycrystalline ceramics having relatively close spectroscopic properties. Based on the detailed spectroscopic study of stoichiometric and binary / ternary solid-solution sesquioxides doped with Tm^{3+} ions performed in the present work, the following conclusions are derived:

(i) Cubic R_2O_3 sesquioxides feature very strong crystal-fields for the Tm^{3+} dopant ions in C_2 symmetry sites which are mainly responsible for their optical properties leading to remarkably high total Stark splitting of their ground-state ($^3H_6$), ranging from 788 cm^{-1} (Y_2O_3) up to 955 cm^{-1} (Sc_2O_3). This leads to broadband emission due to the electronic $^3F_4 \rightarrow {}^3H_6$ transition extending well beyond 2 μm thus avoiding the structured water vapor absorption in the atmospheric air. For $Tm:Sc_2O_3$, the longest wavelength of a purely electronic transition is 2149 nm. In this way, Tm^{3+}-doped sesquioxides can compete with other Ho^{3+}-doped materials.

(ii) The crystal-field strength for the R_2O_3 isostructural series is very sensitive to the nature of the host-forming cation R^{3+} and it increases linearly when decreasing its ionic radius for VI-fold oxygen coordination. The Stark splitting of Tm^{3+} multiplets changes accordingly which enables tuning of the position of emission peaks of Tm^{3+} ions around 2 μm. This trend is valid for both parent and "mixed" compounds.

(iii) The experimental crystal-field splitting for Tm^{3+} ions in C_2 symmetry sites in the parent sesquioxides (Y_2O_3, Lu_2O_3 and Sc_2O_3) is determined for several multiplets relevant for laser applications (from $^3H_6$ to $^3H_4$) and validated using the barycenter plot. The first experimental evidence of C_{3i} Tm^{3+} species for sesquioxides is presented. They are revealed in transitions with a magnetic dipole contribution, $^3H_6 \rightarrow {}^3H_5$ (absorption) and $^3H_4 \rightarrow {}^3H_5$ (emission) while C_{3i} centers do not contribute to the lifetime of the $^3F_4$ upper laser level.

(iv) Based on the X-ray diffraction, Raman spectroscopy and low-temperature absorption / emission spectroscopy, it is confirmed that "mixed" sesquioxide ceramics of the $Y_2O_3 – Lu_2O_3 – Sc_2O_3$ ternary system represent substitutional solid-solutions with mixing of the host-forming cations at the atomic level. This leads to a significant inhomogeneous spectral broadening for the absorption and emission lines of Tm^{3+} ions preserved even at 12 K. The spectral linewidths for "mixed" sesquioxides notably exceed those for the corresponding parent compounds. At ambient temperature, a proper combination of the host-forming cations R^{3+} enables the design

of the gain bandwidth around 2 μm which is of key importance for further pulse shortening in mode-locked lasers. The strongest broadening is observed for Sc^{3+}-containing materials.

(v) Based on the analysis of crystal-field splitting of Tm^{3+} multiplets in various materials, further guidelines for material engineering of gain media for 2 μm mode-locked lasers are given, including the focus on material families forming isostructural series with a notable sensitivity of the crystal-field to the nature of the host-forming cations, in particular those with small ionic radii. Further work in this direction should involve a combination of materials with a structure and / or compositional disorder (for boosting the inhomogeneous spectral broadening leading to a "glassy-like" spectroscopic behavior, i.e., smooth and structureless spectral bands), high crystal-field strength (for broadband emission naturally extending beyond 2 μm), as well as efficient electron-phonon coupling (for utilization of the long-wave phonon sidebands contributing to the extension of the gain bandwidth).

Acknowledgements

French Agence Nationale de la Recherche (ANR) SPLENDID2 (ANR-19-CE08-0028). "RELANCE" Chair of Excellence project funded by the Normandy Region. Contrat de plan État-Région (CPER) de Normandie (France). Russian Science Foundation (research project No. 21-13-00397).

References

1. C. Kränkel, Rare-earth-doped sesquioxides for diode-pumped high-power lasers in the 1-, 2-, and 3-μm spectral range, IEEE J. Sel. Top. Quantum Electron. 21(1), 1602013–1–13 (2015).
2. R. Peters, C. Kränkel, S. T. Fredrich-Thornton, K. Beil, K. Petermann, G. Huber, O. H. Heckl, C. R. E. Baer, C.J. Saraceno, T. Südmeyer, U. Keller, Thermal analysis and efficient high power continuous-wave and mode-locked thin disk laser operation of Yb-doped sesquioxides, Appl. Phys. B 102(3), 509–514 (2011).
3. P. A. Loiko, K. V. Yumashev, R. Schödel, M. Peltz, C. Liebald, X. Mateos, B. Deppe, C. Kränkel, Thermo-optic properties of Yb:Lu_2O_3 single crystals, Appl. Phys. B 120(4), 601–607 (2015).
4. M. V. Abrashev, N. D. Todorov, J. Geshev, Raman spectra of R_2O_3 (R—rare earth) sesquioxides with C-type bixbyite crystal structure: A comparative study, J. Appl. Phys. 116(10), 103508–1–7 (2014).
5. P. Loiko, P. Koopmann, X. Mateos, J. M. Serres, V. Jambunathan, A. Lucianetti, T. Mocek, M. Aguiló, F. Díaz, U. Griebner, V. Petrov, C. Kränkel, Highly-efficient, compact Tm^{3+}:RE_2O_3 (RE = Y, Lu, Sc) sesquioxide lasers based on thermal guiding, IEEE J. Sel. Top. Quantum Electron. 24(5), 1600713–1–13 (2018).
6. M. J. Weber, Radiative and multiphonon relaxation of rare-earth ions in Y_2O_3, Phys. Rev. 171(2), 283–291 (1968).
7. F. Hanic, M. Hartmanová, G.G. Knab, A.A. Urusovskaya, K.S. Bagdasarov, Real structure of undoped Y_2O_3 single crystals, Acta. Crystallogr. B. Struct. Sci. Cryst. Eng. Mater. 40(2), 76–82 (1984).
8. M. Faucher J. Pannetier, Refinement of the Y_2O_3 structure at 77 K, Acta Crystallogr. B: Struct. Crystallogr. Cryst. Chem. 36(12), 3209–3211 (1980).

9. S. So, J. I. Mackenzie, D. P. Shepherd, W. A. Clarkson, J. G. Betterton, E. K. Gorton, A power-scaling strategy for longitudinally diode-pumped Tm:YLF lasers, Appl. Phys. B 84(3), 389–393 (2006).
10. E. C. Honea, R. J. Beach, S. B. Sutton, J. A. Speth, S. C. Mitchell, J. A. Skidmore, M. A. Emanuel, S. A. Payne, 115-W Tm:YAG diode-pumped solid-state laser, IEEE J. Quantum Electron. 33(9), 1592–1600 (1997).
11. K. Van Dalfsen, S. Aravazhi, C. Grivas, S. M. García-Blanco, M. Pollnau, Thulium channel waveguide laser with 1.6 W of output power and ~80% slope efficiency, Opt. Lett. 39(15), 4380–4383 (2014).
12. Y. Guyot, R. Moncorgé, L. D. Merkle, A. Pinto, B. McIntosh, H. Verdun, Luminescence properties of Y_2O_3 single crystals doped with Pr^{3+} or Tm^{3+} and codoped with Yb^{3+}, Tb^{3+} or Ho^{3+} ions, Opt. Mater. 5(1-2), 127–136 (1996).
13. A. Suzuki, C. Kränkel, M. Tokurakawa, High quality-factor Kerr-lens mode-locked Tm:Sc_2O_3 single crystal laser with anomalous spectral broadening, Appl. Phys. Express 13(5), 052007–1–4 (2020).
14. Y. Zhao, L. Wang, Y. Wang, J. Zhang, P. Liu, X. Xu, Y. Liu, D. Shen, J. E. Bae, T. G. Park, F. Rotermund, X. Mateos, P. Loiko, Z. Wang, X. Xu, J. Xu, M. Mero, U. Griebner, V. Petrov, W. Chen, SWCNT-SA mode-locked Tm:$LuYO_3$ ceramic laser delivering 8-optical-cycle pulses at 2.05 μm, Opt. Lett. 45(2), 459–462 (2020).
15. P. Koopmann, R. Peters, K. Petermann, G. Huber, Crystal growth, spectroscopy, and highly efficient laser operation of thulium-doped Lu_2O_3 around 2 μm, Appl. Phys. B 102(1), 19–24 (2011).
16. L. Zheng, H. Wu, L. Zhang, Y. Luo, G. H. Pan, X. J. Wang, Z. Hao, J. Zhang, Determination of cross-relaxation efficiency based on spectroscopy in thulium-doped rare-earth sesquioxides, Ceram. Int. 49(7), 11060–11066 (2023).
17. O. L. Antipov, A. A. Novikov, N. G. Zakharov, A. P. Zinov'ev, Optical properties and efficient laser oscillation at 2066 nm of novel Tm:Lu_2O_3 ceramics, Opt. Mater. Express 2(2), 183–189 (2012).
18. F. Auzel O. L. Malta, A scalar crystal field strength parameter for rare-earth ions: meaning and usefulness, J. Physique 44(2), 201–206 (1983).
19. C. Kränkel, A. Uvarova, É. Haurat, L. Hülshoff, M. Brützam, C. Guguschev, S. Kalusniak, D. Klimm, Czochralski growth of mixed cubic sesquioxide crystals in the ternary system Lu_2O_3–Sc_2O_3–Y_2O_3, Acta. Crystallogr. B. Struct. Sci. Cryst. Eng. Mater. 77(4), 550–558 (2021).
20. W. Jing, P. Loiko, J. Maria Serres, Y. Wang, E. Vilejshikova, M. Aguiló, F. Díaz, U. Griebner, H. Huang, V. Petrov, X. Mateos, Synthesis, spectroscopy, and efficient laser operation of mixed sesquioxide Tm:$(Lu,Sc)_2O_3$ transparent ceramics, Opt. Mater. Express 7(11), 4192–4202 (2017).
21. K. Eremeev, P. Loiko, A. Braud, P. Camy, J. Zhang, X. Xu, Y. Zhao, P. Liu, S. Balabanov, E. Dunina, A. Kornienko, Spectroscopy of solid-solution transparent sesquioxide laser ceramic Tm:$LuYO_3$, Opt. Mater. Express 12(9), 3749–3762 (2022).
22. Y. Zhao, L. Wang, W. Chen, Z. Pan, Y. Wang, P. Liu, X. Xu, Y. Liu, D. Shen, J. Zhang, M. Guina, X. Mateos, P. Loiko, Z. Wang, X. Xu, J. Xu, M. Mero, U. Griebner, V. Petrov, SESAM mode-locked Tm:$LuYO_3$ ceramic laser generating 54-fs pulses at 2048 nm, Appl. Opt. 59(33), 10493–10497 (2020).

23. Z. Liu, A. Ikesue, J. Li, Research progress and prospects of rare-earth doped sesquioxide laser ceramics, J. Eur. Ceram. Soc. 41(7), 3895–3910 (2021).
24. A. Suzuki, S. Kalusniak, H. Tanaka, M. Brützam, S. Ganschow, M. Tokurakawa, C. Kränkel, Spectroscopy and 2.1 μm laser operation of Czochralski-grown Tm^{3+}:$YScO_3$ crystals, Opt. Express 30(23), 42762–42771 (2022).
25. C. Kränkel, A. Uvarova, C. Guguschev, S. Kalusniak, L. Hülshoff, H. Tanaka, D. Klimm, Rare-earth doped mixed sesquioxides for ultrafast lasers, Opt. Mater. Express 12(3), 1074–1091 (2022).
26. L. Pauling, M.D. Shappell, The crystal structure of bixbyite and the C-modification of the sesquioxides, Z. fur Krist. - Cryst. Mater. 75(1), 128–142 (1930).
27. R. D. Shannon, Revised effective ionic radii and systematic studies of interatomic distances in halides and chalcogenides, Acta Crystallogr. A: Cryst. Phys. Diffr. Theor. Gen. Crystallogr. 32(5), 751–767 (1976).
28. L. Vegard, Die konstitution der mischkristalle und die raumfüllung der atome, Z. fur Physik 5(1), 17–26 (1921).
29. Y. Repelin, C. Proust, E. Husson, J. M. Beny, Vibrational spectroscopy of the C-form of yttrium sesquioxide, J. Solid State Chem. 118(1), 163–169 (1995).
30. N. D. Todorov, M. V. Abrashev, V. Marinova, M. Kadiyski, L. Dimowa, E. Faulques, Raman spectroscopy and lattice dynamical calculations of Sc_2O_3 single crystals, Phys. Rev. B 87(10), 104301–1–5 (2013).
31. R. Moncorgé, Y. Guyot, C. Kränkel, K. Lebbou, A. Yoshikawa, Mid-infrared emission properties of the Tm^{3+}-doped sesquioxide crystals Y_2O_3, Lu_2O_3, Sc_2O_3 and mixed compounds (Y, Lu, Sc)$_2O_3$ around 1.5-, 2-and 2.3-μm, J. Lum. 241, 118537–1–9 (2022).
32. B. F. Aull H. P. Jenssen, Vibronic interactions in Nd:YAG resulting in nonreciprocity of absorption and stimulated emission cross sections, IEEE J. Quantum Electron. 18(5), 925–930 (1982).
33. D. E. Zelmon, J. M. Northridge, N. D. Haynes, D. Perlov, K. Petermann, Temperature-dependent Sellmeier equations for rare-earth sesquioxides, Appl. Opt. 52(16), 3824–3828 (2013).
34. S. A. Payne, L. L. Chase, L. K. Smith, W. L. Kway, W. F. Krupke, Infrared cross-section measurements for crystals doped with Er^{3+}, Tm^{3+} and Ho^{3+}, IEEE J. Quantum Electron. 28(11), 2619–2630 (1992).
35. Y. Wang, G. Xie, X. Xu, J. Di, Z. Qin, S. Suomalainen, M. Guina, A. Härkönen, A. Agnesi, U. Griebner, X. Mateos, SESAM mode-locked Tm:CALGO laser at 2 μm, Opt. Mater. Express 6(1), 131–136 (2016).
36. P. Loiko, J.M. Serres, X. Mateos, K. Yumashev, N. Kuleshov, V. Petrov, U. Griebner, M. Aguiló, F. Díaz, Microchip laser operation of Tm,Ho:$KLu(WO_4)_2$ crystal, Opt. Express 22(23), 27976–27984 (2014).
37. F. Auzel, Multiphonon-assisted anti-Stokes and Stokes fluorescence of triply ionized rare-earth ions, Phys. Rev. B 13(7), 2809–2817 (1976).
38. Y. Zhao, L. Wang, W. Chen, P. Loiko, Y. Wang, Z. Pan, H. Yang, W. Jing, H. Huang, J. Liu, X. Mateos, Kerr-lens mode-locked Tm-doped sesquioxide ceramic laser, Opt. Lett. 46(14), 3428–3431 (2021).
39. P. Loiko M. Pollnau, Stochastic model of energy-transfer processes among rare-earth ions. Example of Al_2O_3: Tm^{3+}, J. Phys. Chem. C 120(46), 26480–26489 (2016).

40. R. P. Leavitt, J. B. Gruber, N. C. Chang, C. A. Morrison, Optical spectra, energy levels, and crystal-field analysis of tripositive rare-earth ions in Y_2O_3. II. Non-Kramers ions in C_2 sites, J. Chem. Phys. 76(10), 4775–4788 (1982).
41. J. B. Gruber, R. P. Leavitt, C. A. Morrison, N. C. Chang, Optical spectra, energy levels, and crystal-field analysis of tripositive rare-earth ions in Y_2O_3. IV. C_{3i} sites, J. Chem. Phys. 82(12), 5373–5378 (1985).
42. J. B. Gruber, W. F. Krupke, J. M. Poindexter, Crystal-field splitting of trivalent thulium and erbium J levels in yttrium oxide, J. Chem. Phys. 41(11), 3363–3377 (1964).
43. A. Uvarova, P. Loiko, S. Kalusniak, E. Dunina, L. Fomicheva, A. Kornienko, S. Balabanov, A. Braud, P. Camy, C. Kränkel, Stimulated-emission cross-sections of trivalent erbium ions in the cubic sesquioxides Y_2O_3, Lu_2O_3, and Sc_2O_3, Opt. Mater. Express 13(5), 1385–1400 (2023).
44. L. Fornasiero, Nd^{3+} - und Tm^{3+} -dotierte sesquioxide, Ph.D. dissertation, Dept. Phys., Univ. Hamburg, Hamburg, Germany (1999).
45. P. Koopmann, Thulium- and holmium-doped sesquioxides for 2 μm lasers, Ph.D. dissertation, Dept. Phys., Univ. Hamburg, Hamburg, Germany (2012).
46. P. H. Haumesser, R. Gaume, B. Viana, E. Antic-Fidancev, D. Vivien, Spectroscopic and crystal-field analysis of new Yb-doped laser materials, J. Condens. Matter Phys. 13(23), 5427–5447 (2001).
47. E. Antic-Fidancev, Simple way to test the validity of $^{2S+1}L_J$ barycenters of rare earth ions (e.g. $4f^2$, $4f^3$ and $4f^6$ configurations), J. Alloys Compd. 300, 2–10 (2000).
48. A.A. Kaminskii, Laser crystals their physics and properties, 14 Springer (2013).
49. E. Antic-Fidancev, J. Hölsä, M. Lastusaari, Crystal field strength in C-type cubic rare earth oxides, J. Alloys Compd. 341(1-2), 82–86 (2002).
50. E. Antic-Fidancev, M. Lemaître-Blaise, P. Porcher, Optical study of praseodymium 3+ in zircon-type orthovanadate phases, Spectrochim. Acta A: Mol. Biomol. Spectrosc. 54(13), 2151–2156 (1998).
51. J. Hölsä, R.J. Lamminmäki, M. Lastusaari, P. Porcher, R.S. Puche, Simulation of the spectroscopic and magnetic properties of RE (III) ions in RE oxychlorides based on exact crystal structure from Rietveld refinements, J. Alloys Compd. 300, 45–54 (2000).
52. P. Loiko, Y. Wang, J.M. Serres, X. Mateos, M. Aguilo, F. Diaz, L. Zhang, Z. Lin, H. Lin, G. Zhang, E. Vilejshikova, Monoclinic Tm:$MgWO_4$ crystal: Crystal-field analysis, tunable and vibronic laser demonstration, J. Alloys Compd. 763, 581–591 (2018).
53. N. Zhang, Q. Song, J. Zhou, J. Liu, S. Liu, H. Zhang, X. Xu, Y. Xue, J. Xu, W. Chen, Y. Zhao, 44-fs pulse generation at 2.05 μm from a SESAM mode-locked Tm:$GdScO_3$ laser, Opt. Lett. 48(2), 510–513 (2023).

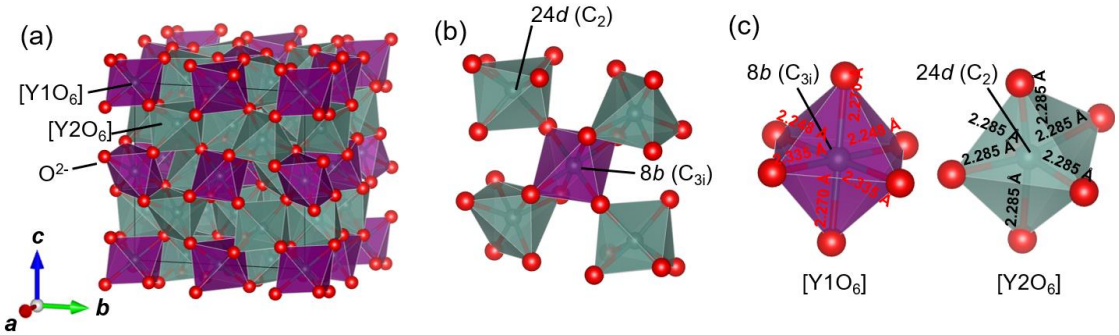

Figure 1. The crystal structure of C-type Y_2O_3: (a) a fragment of the crystal structure, *black lines* – unit-cell; (b) the connection between the [Y1O$_6$] and [Y2O$_6$] polyhedra; (c) the local geometry of the C_2 and C_{3i} symmetry sites.

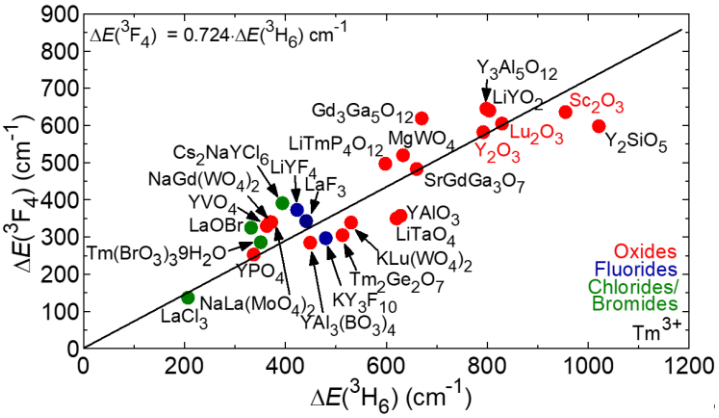

Figure 2. Total Stark splitting of the first excited-state ($^3F_4$) vs. that of the ground-state ($^3H_6$) for Tm^{3+} ions in various crystals (oxide (*red*), fluoride (*blue*) and chloride / bromide (*green*)), *symbols* – experimental data from the literature, *line* – their linear fit. For cubic sesquioxides, C_2 sites are considered.

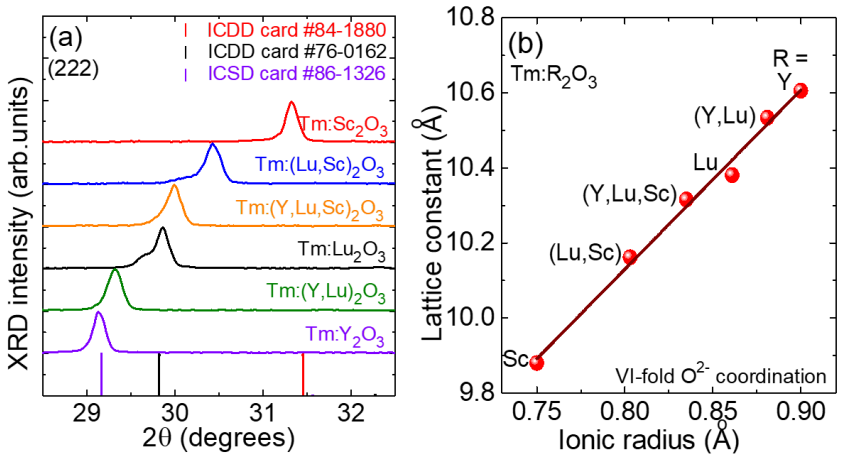

Figure 3. X-ray powder diffraction (XRD) study of 3 at.% $Tm:R_2O_3$ ceramics (R = Y, Lu, Sc or their mixture): (a) a close look at the (222) diffraction peak; (b) the lattice constant *a* as a function of the average ionic radius of the host-forming cations R^{3+} (for VI-fold oxygen coordination).

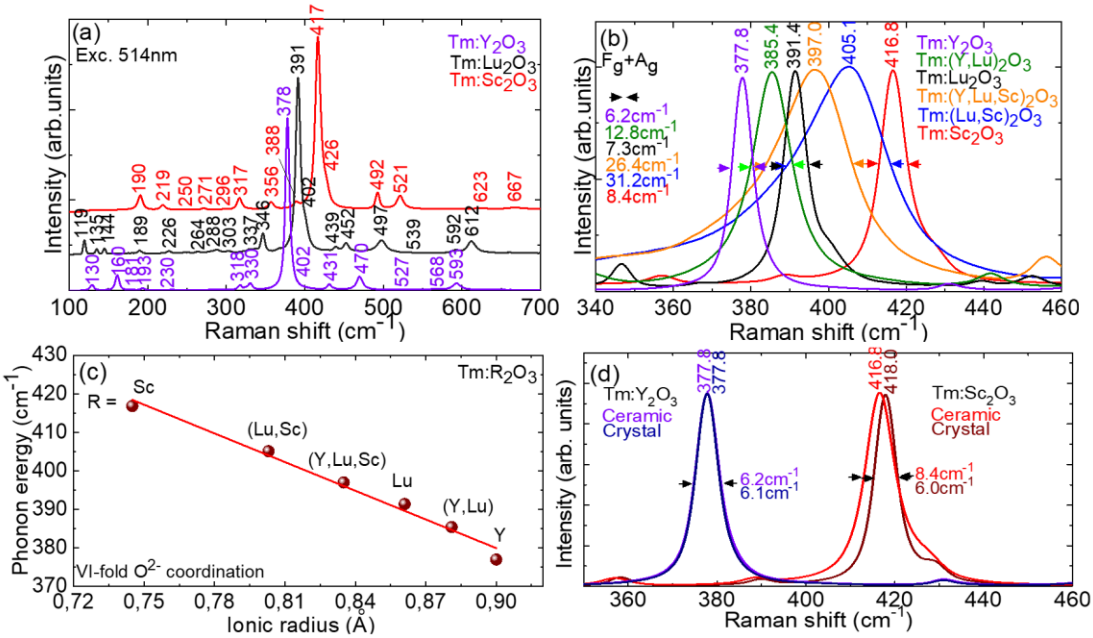

Figure 4. Raman spectroscopy of 3 at.% $Tm:R_2O_3$ ceramics (R = Y, Lu, Sc or their mixture): (a) overview Raman spectra of $Tm:Y_2O_3$, $Tm:Lu_2O_3$ and $Tm:Sc_2O_3$ ceramics; (b) a close look at the most intense mode ($F_g + A_g$); (c) its phonon energy vs. the ionic radius of the host-forming R^{3+} cation (VI-fold oxygen coordination); (d) a comparison of the Raman spectra of $Tm:Y_2O_3$ and $Tm:Sc_2O_3$ single-crystals and ceramics. λ_{exc} = 514 nm.

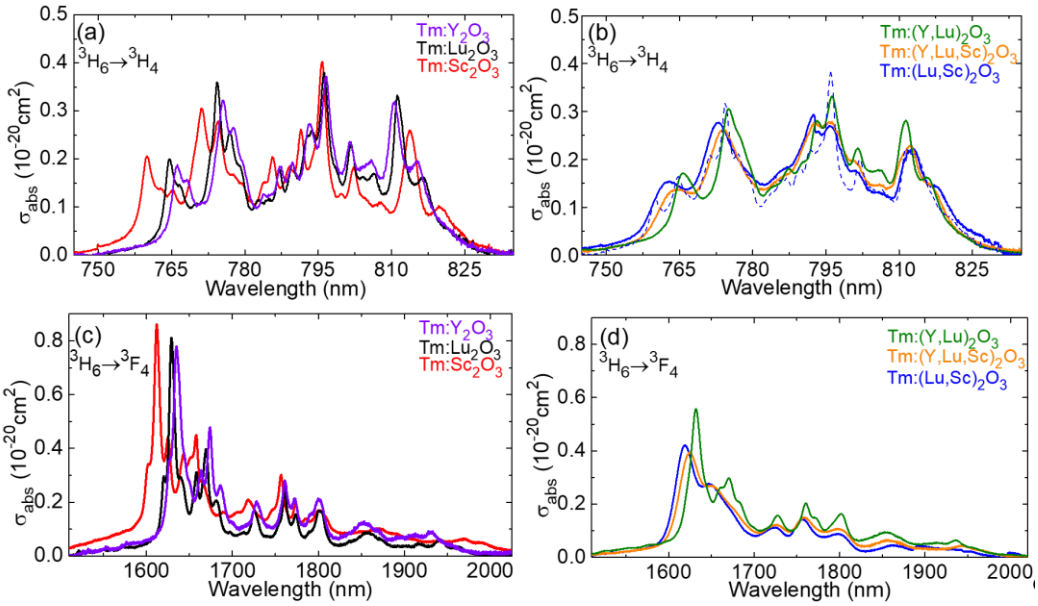

Figure 5. RT absorption cross-sections, σ_{abs}, for (a,b) the $^3H_6 \rightarrow {}^3H_4$ transition and (c,d) the $^3H_6 \rightarrow {}^3F_4$ transition of Tm^{3+} ions in the R_2O_3 ceramics (R = Y, Lu, Sc or their mixture). *Dashed curve* in (b) – linear combination of Tm^{3+} absorption spectra in Lu_2O_3 and Sc_2O_3.

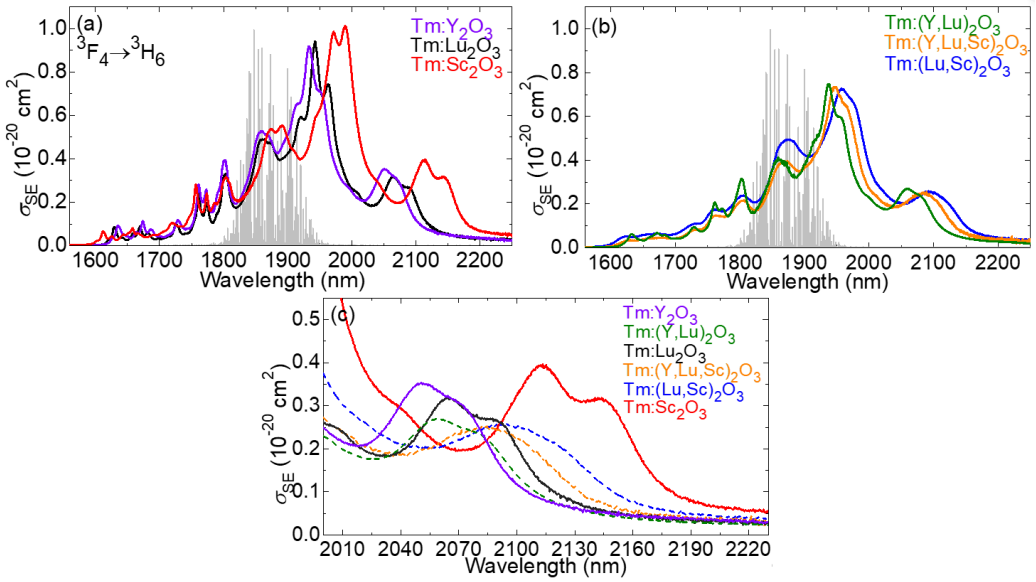

Figure 6. RT stimulated-emission (SE) cross-section, σ_{SE}, spectra for the $^3F_4 \rightarrow {}^3H_6$ transition of Tm^{3+} ions in the R_2O_3 ceramics (R = Y, Lu, Sc or their mixture): (a) parent compounds; (b) solid-solution compositions; (c) a close look at the 2000-2230 nm range. *Grey lines* – water absorption according to the HITRAN database [arb. units].

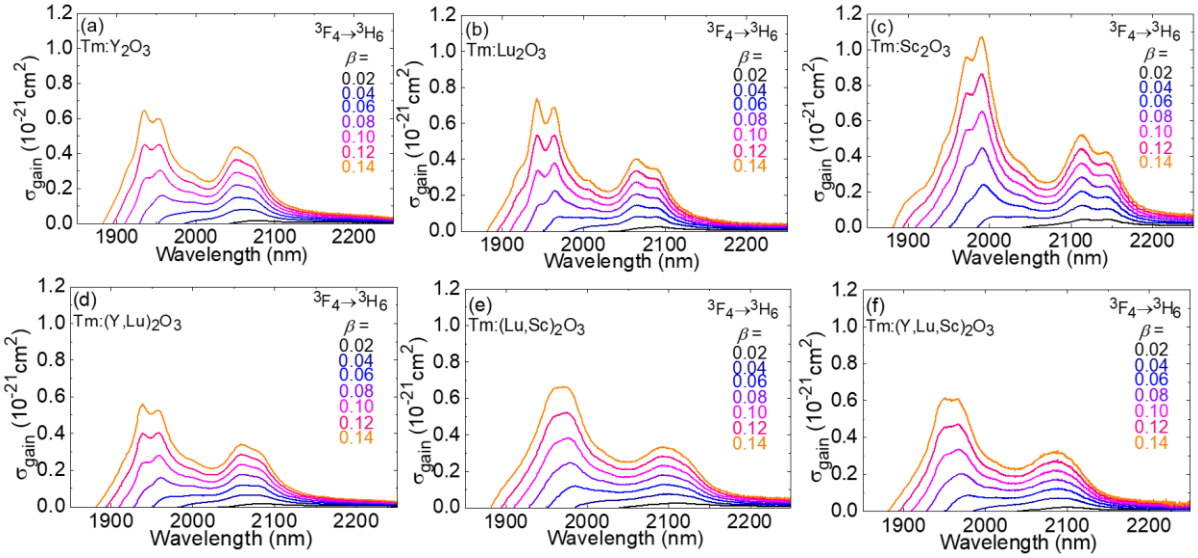

Figure 7. (a-f) Gain cross-section, $\sigma_{gain} = \beta\sigma_{SE} - (1 - \beta)\sigma_{abs}$, spectra for Tm^{3+} ions in the R_2O_3 ceramics (R = Y, Lu, Sc or their mixture), plotted for different inversion ratios $\beta = N_2(^3F_4)/N_{Tm}$.

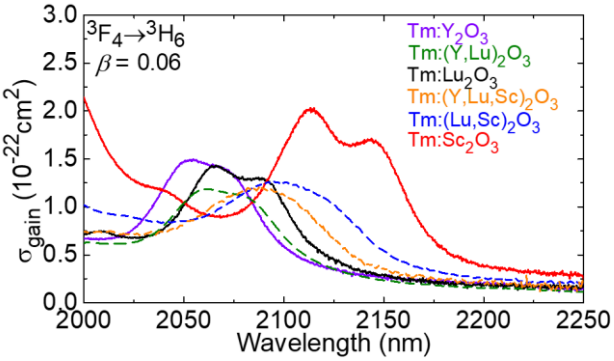

Figure 8. A comparison of gain profiles of Tm^{3+} ions in the R_2O_3 ceramics (R = Y, Lu, Sc or their mixture) in the spectral range of 2000 – 2250 nm, for a fixed inversion ratio β = 0.06.

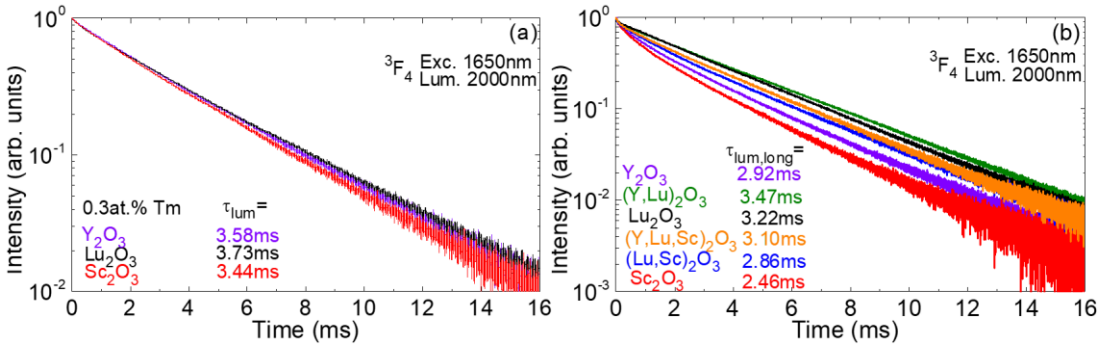

Figure 9. RT luminescence decay curves from the $^3F_4$ Tm^{3+} state in Tm:R_2O_3 ceramics (R = Y, Lu, Sc or their mixture): (a) 0.3 at.% Tm, parents, (b) 3 at.% Tm, all compositions, λ_{exc} = 1650 nm, λ_{lum} = 2000 nm. Powdered samples. In (b), $\tau_{lum,long}$ corresponds to the long time component of the decay.

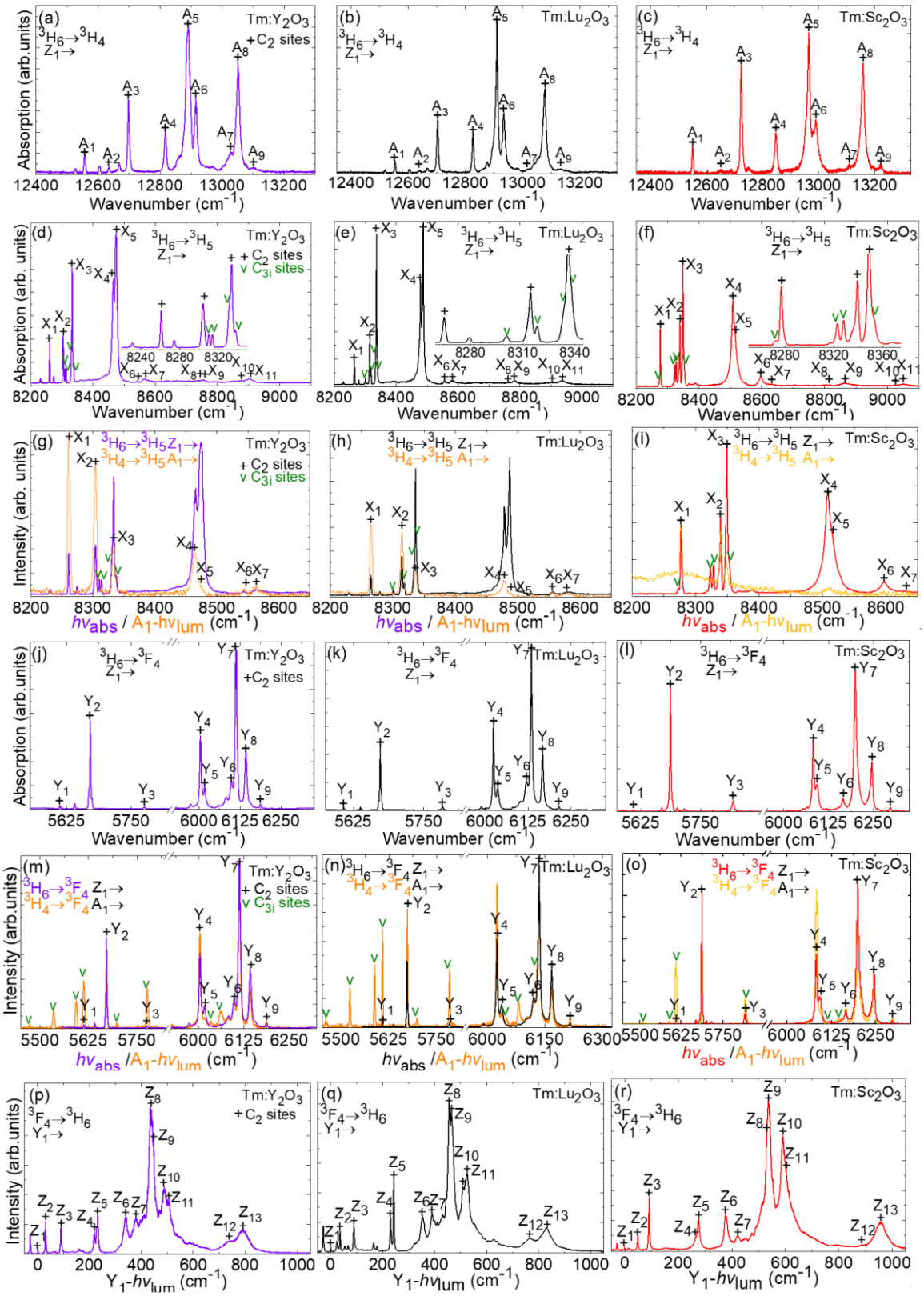

Figure 10. LT (12 K) absorption and emission spectra of Tm^{3+} ions in (a,d,g,j,m,p) Y_2O_3, (b,e,h,k,n,q) Lu_2O_3 and (c,f,i,l,o,r) Sc_2O_3 crystals: (a-c) the $^3H_6 \rightarrow {}^3H_4$ transition; (d-f) the $^3H_6 \rightarrow {}^3H_5$ transition; (g-i) the $^3H_6 \rightarrow {}^3F_4$ transition; (g-i) $^3H_6 \rightarrow {}^3H_5$ and $^3H_4 \rightarrow {}^3H_5$, (m-o) the $^3H_6 \rightarrow {}^3F_4$ and $^3H_4 \rightarrow {}^3F_4$ transitions and (p-r) the $^3F_4 \rightarrow {}^3H_6$ transitions, + – C_2 sites, v – C_{3i} sites.

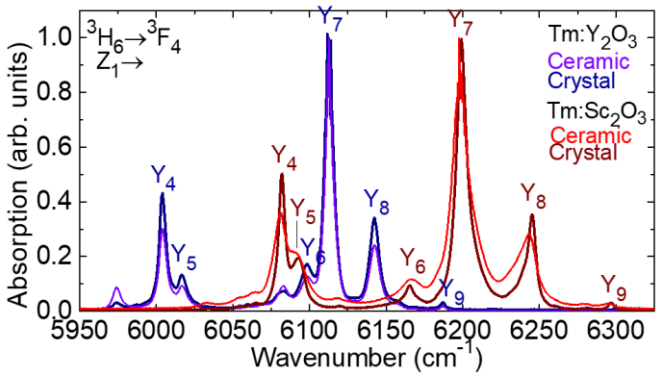

Figure 11. A comparison of LT (12 K) absorption spectra of Tm^{3+} ions (the $^3H_6 \rightarrow {}^3F_4$ transition) in Y_2O_3 and Sc_2O_3 single crystals and ceramics. Y_i denote electronic transitions to the Stark sub-levels of the $^3F_4$ multiplet.

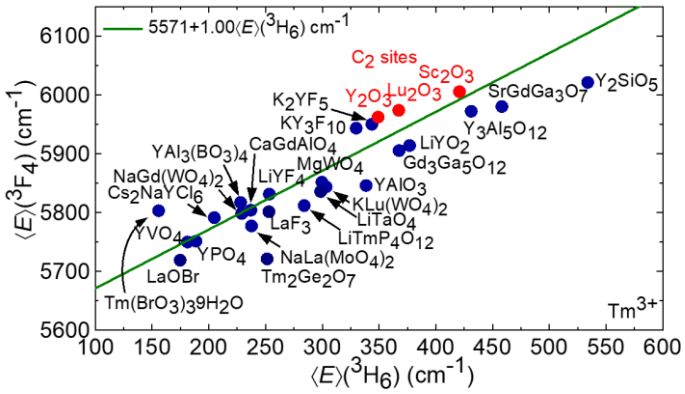

Figure 12. A barycenter plot of the crystal-field splitting for Tm^{3+} ions in various hosts: the barycenter energy $\langle E \rangle$, of the $^3F_4$ excited-state versus that of the $^3H_6$ ground-state, plotted along the nephelauxetic scale. *symbols* – experimental data, *line* – their phenomenological fit. *Red circles* – data for cubic sesquioxides (C_2 sites).

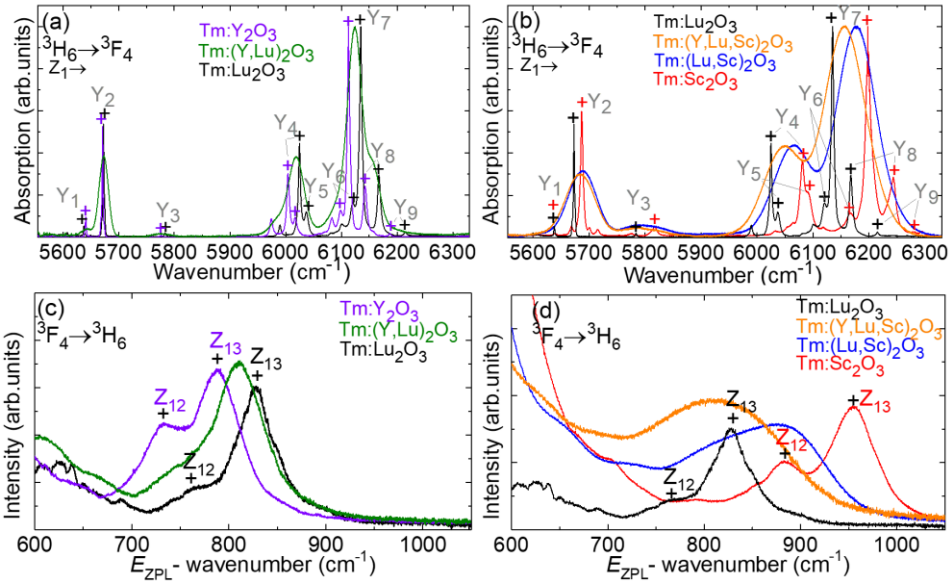

Figure 13. Inhomogenous spectral broadening for Tm^{3+} ions in "mixed" sesquioxide ceramics: (a,c) Y_2O_3 – Lu_2O_3 binary system; (b,d) Lu_2O_3 – Sc_2O_3 binary and Y_2O_3 – Lu_2O_3 – Sc_2O_3 ternary systems, (a,b) the $^3H_6 \rightarrow {}^3F_4$ transition in absorption; (c,d) the $^3F_4 \rightarrow {}^3H_6$ transition in 25mission, a close look at the spectral range above 2 μm relevant for laser operation.

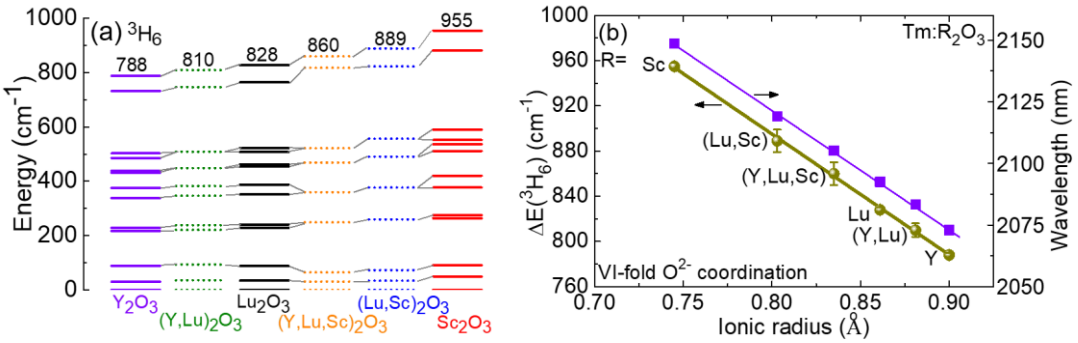

Figure 14. (a) The experimental crystal-field splitting of the $^3H_6$ Tm^{3+} multiplet in 3 at.% Tm:R_2O_3 (R = Y, Lu, Sc or their mixture); (b) the total ground-state Stark splitting and the longest wavelength of the purely electronic transition $^3F_4 \rightarrow {}^3H_6$ vs. the average R^{3+} ionic radius for VI-fold oxygen coordination.

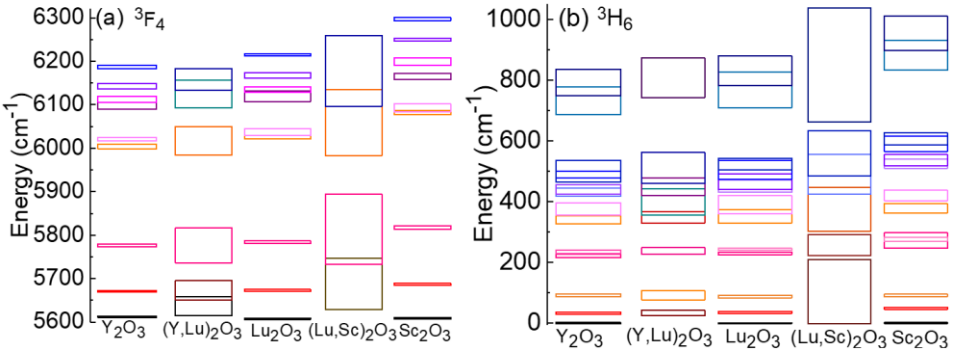

Figure 15. Inhomogeneous broadening of the energy-levels of the ground-state $^3H_6$ and the first excited-state $^3F_4$ of Tm^{3+} ions in Tm:R_2O_3 (R = Y, Lu, Sc or their mixture) ceramics (at 12 K) by the crystal field. The height of each rectange corresponds to the FWHM of the absorption / emission peaks corresponding to individual electronic transitions.

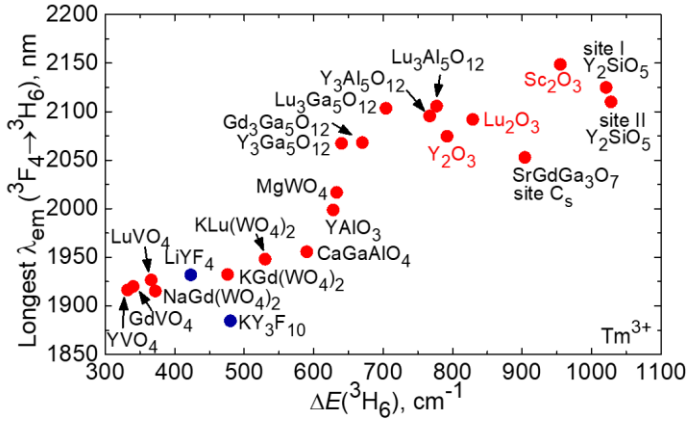

Figure 16. The longest wavelength corresponding to the purely electronic transition $^3F_4 \rightarrow {}^3H_6$ vs. the total Stark spitting ΔE of the $^3H_6$ ground-state for Tm^{3+} ions in various crystalline matrices considered for mode-locked lasers at ~2 μm.

Table 1. Peak absorption and stimulated-emission cross-sections for Thulium ions in R_2O_3 ceramics.

R_2O_3	σ_{abs}, 10^{-20} cm^2	λ_{abs}, nm	$\Delta\lambda_{abs}$, nm	σ_{SE}, 10^{-20} cm^2	λ_{lum}, nm	$\Delta\lambda_{lum}$, nm	Z_1/Z_2
Y_2O_3	0.37	796.7	4.2	0.35	2051.6	50.2	1.429
Lu_2O_3	0.38	796.2	3.5	0.32	2064.4	58.1	1.445
Sc_2O_3	0.40	795.8	3.4	0.39	2113.7	64.1	1.447
$(Y,Lu)_2O_3$	0.33	796.2	~21	0.27	2059.0	54.7	
$(Y,Lu,Sc)_2O_3$	0.28	796.0	~21	0.25	2087.9	63.0	
$(Lu,Sc)_2O_3$	0.29	792.2	~21	0.26	2095.7	69.8	

Table 2. Intrinsic luminescence ($\tau_{lum,0}$) and radiative (τ_{rad}) lifetimes of the $^3F_4$ Tm^{3+} multiplet in Y_2O_3, Lu_2O_3 and Sc_2O_3.

Compound	$\tau_{lum,0}$, ms ceramic	$\tau_{lum,0}$, ms [5] crystal	τ_{rad}, ms [31]
$Tm:Y_2O_3$	3.58	3.54	3.79
$Tm:Lu_2O_3$	3.73	3.38	3.84
$Tm:Sc_2O_3$	3.44	3.57	3.80

Table 3. Experimental crystal-field splitting of Tm^{3+} multiplets in Y_2O_3, Lu_2O_3 and Sc_2O_3 (C_2 and C_{3i} sites).

R_2O_3	$^{2S+1}L_J$	Notation	E, cm^{-1}
Y_2O_3	$^3H_6$	Z	0; 30; 89; 217; 229; 338; 376; 432; 439; 486; 503; 732; 788 (C_2)
			0; 37; 130; 213; 384; 519; 709; 761; 762 (C_{3i}) [42]
	$^3F_4$	Y	5612; 5672; 5776; 6003; 6016; 6099; 6112; 6142; 6187 (C_2)
			5472; 5535; 5593; 5612; 5696; 5776; 6034; 6060 (C_{3i})
	$^3H_5$	X	8261; 8304; 8333; 8466; 8474; 8542; 8562; 8742; 8755; 8875; 8905 (C_2)
			8310; 8314; 8331; 8338 (C_{3i})
	$^3H_4$	A	12557; 12634; 12698; 12817; 12890; 12915; 13028; 13051; 13103 (C_2)
Lu_2O_3	$^3H_6$	Z	0; 35; 88; 229; 241; 352; 388; 455; 463; 508; 523; 764; 828 (C_2)
	$^3F_4$	Y	5607; 5673; 5784; 6025; 6037; 6120; 6135; 6167; 6214 (C_2)
			5461; 5522; 5588; 5608; 5698; 5784; 6050; 6082; 6130 (C_{3i})
	$^3H_5$	X	8265; 8315; 8336; 8479; 8487; 8556; 8580; 8761; 8783; 8900; 8937 (C_2)
			8301; 8318; 8334; 8339 (C_{3i})
	$^3H_4$	A	12553; 12640; 12703; 12826; 12910; 12934; 13016; 13078; 13135 (C_2)
Sc_2O_3	$^3H_6$	Z	0; 49; 91; 265; 275; 377; 422; 529; 537; 590; 607; 882; 955 (C_2)
	$^3F_4$	Y	5609; 5687; 5818; 6082; 6093; 6166; 6199; 6245; 6296 (C_2)
			5510; 5587; 5609; 5818; 6111; 6143 (C_{3i})
	$^3H_5$	X	8278; 8339; 8349; 8508; 8515; 8598; 8632; 8809; 8863; 9020; 9052 (C_2)
			8272; 8323; 8328; 8353 (C_{3i})
	$^3H_4$	A	12550; 12650; 12725; 12848; 12966; 12991; 13111; 13160; 13222 (C_2)